Liquid Water Path and Plane-Parallel Albedo Bias during ASTEX

ROBERT F. CAHALAN AND DAVID SILBERSTEIN*

NASA/Goddard Space Flight Center, Laboratory for Atmospheres, Greenbelt, Maryland

JACK B. SNIDER

NOAA/ERL/Environmental Technology Laboratory, Boulder, Colorado

(Manuscript received 8 July 1994, in final form 29 December 1994)

ABSTRACT

Inhomogeneous distributions of liquid water like those observed in real clouds generally reflect less solar radiation than idealized uniform distributions assumed in plane-parallel theory. Here the authors determine cloud reflectivity and the associated plane-parallel albedo bias from distributions of liquid water path derived from 28 days of microwave radiometer measurements obtained on Porto Santo Island in the Madeiras during June 1992 as part of the Atlantic Stratocumulus Transition Experiment (ASTEX). The distributions are determined for each hour of the day, both for composites of the full set of 28 days and for a subset of 8 days having a high fraction of relatively thick cloud. Both sets are compared with results obtained from California stratocumulus during FIRE [First ISCCP (International Satellite Cloud Climatology Project) Regional Experiment].

In FIRE the albedo bias was dominated by the variability of the cloud optical depth, as measured by a fractal parameter, $0 \leq f \leq 1$, while the ASTEX results are more complex. Mean cloud fraction above a 10 g m^{-2} threshold is about 50% in the 28-day set, compared to 76% in the 8-day subset and 82% in FIRE. Cloud fraction is sensitive to the threshold for the 28 ASTEX days, probably due to a large fraction of thin cloud below the threshold, but this is not the case for the 8-day subset or for FIRE. Clear fractions during ASTEX are generally of shorter duration than those in FIRE, as are those in the 8-day subset. The diurnal mean fractal parameter is about 0.6 in ASTEX compared to 0.5 in FIRE, while the 8-day subset has nearly the same mean but a wider range. The diurnal cycle in cloud albedo and albedo bias is computed from the cloud parameters for both sets, assuming zero clear-sky albedo. The total absolute albedo bias rises to values above 0.3 at sunrise and sunset, but since there is little incident energy at that time, the reflected flux is more affected by the midday bias. The total albedo bias has a 1000 LST maximum of about 0.3, largely due to a cloud fraction contribution of 0.2, absent in FIRE because in that case cloud fraction remains near 100% until after 1000 LST. The albedo bias has a second maximum of about 0.2 at noon, again mainly from cloud fraction, and then drops to a minimum of about 0.1 at 1400 LST, when cloud fraction and fractal structure contribute about equally. Finally, a third maximum due to cloud fraction occurs at 1600 LST.

In the 8-day subset, the 1000 LST maximum becomes dominated by the fractal structure, since the cloud fraction remains near 100% until 1000 LST, as in FIRE. The noon maximum receives roughly equal contributions, while the 1400 LST minimum bias is mainly due to fractal structure. Finally, the 1600 LST maximum and the evening limb bias are similar to those of the full 28-day set. These results show that cloud fractal and radiative properties can vary considerably from one site and time to another, and at different times within the same site, as meteorological conditions change.

1. Introduction

Computations based on observations of California stratocumulus during FIRE [First ISCCP (International Satellite Cloud Climatology Project) Regional Experiment] have shown that stratocumulus have significant fractal structure and that this "within-cloud" structure can have a greater impact on average albedo than cloud fraction (Cahalan and Snider 1989; Cahalan 1994; Cahalan et al. 1994a; Cahalan et al. 1994b). These studies distribute the cloud liquid by a "bounded cascade," in which a fraction $0 \leq f * c^n \leq 1$ of liquid water is transferred at cascade step n and the parameters c and f are adjusted to fit the scaling exponent of the power spectrum of liquid water path W and the standard deviation of $\log(W)$, respectively. [Scaling properties of this model were discussed by Marshak et al. (1994).] The bias in plane-parallel albedo estimates was determined from the model as an analytic function of c and f, as well as the cloud fraction A_c, mean vertical cloud optical thickness τ_v, and sun angle θ_0. For values typical of the diurnal mean in FIRE ($c \approx 0.8$, $f \approx 0.5$,

* Additional affiliation: Hughes-STX, Lanham, Maryland.

Corresponding author address: Dr. Robert F. Cahalan, Code 913, Laboratory for Atmospheres, Goddard Space Flight Center, Greenbelt, MD 20771.

$A_c \approx 0.8$, $\tau_v \approx 15$, and $\theta_0 \approx 60°$) the absolute bias was found to be about 0.09, or 15% of the plane-parallel albedo of 0.69. A surprising result of the FIRE study was that the largest bias occurs in the morning when $A_c \approx 1$, so that the bias is dominated by the within-cloud fractal structure.

The purpose of this paper is to study the plane-parallel albedo bias as a function of time of day during the Atlantic Stratocumulus Transition Experiment (ASTEX) in the Azores–Madeira Island region during June 1992. Like the FIRE region over the subtropical Pacific off California, the ASTEX region is usually controlled by a subtropical inversion in summer, the wind is generally northerly, and the clouds are mainly a mixture of stratocumulus and fair weather cumulus. However, the meteorology of the ASTEX region is much more varied than that off California. Coastal California has influences such as the "Catalina Eddy," but away from the coast in summer the northerly wind is relatively persistent, and the cloud climatology consists primarily of a high fraction of marine stratocumulus. By contrast, the ASTEX region in summer experiences frequent incursions of midlatitude or tropical disturbances, which produce clouds having significant vertical development, sometimes with overlying cirrus, so that the relatively simple boundary layer structure is replaced by multilayer structures sometimes extending to the tropopause. As a result, the distributions of cloud liquid water and the resulting cloud radiative properties are quite different in ASTEX than in FIRE, as we shall see. In particular, we show that while mean cloud liquid water and optical thickness in ASTEX are similar to that in FIRE, there is wider variability due to a greater percentage of both thicker and thinner cloud. The cloud fraction is also much lower, and the albedo bias in ASTEX is more strongly influenced by cloud fraction, although the within-cloud fractal structure also makes a significant contribution, especially on days having a high fraction of relatively thick cloud.

The results presented here reinforce earlier studies showing that cloud fraction alone is insufficient to parameterize dependence of the large-scale albedo and other radiative properties on subgrid-scale cloud structure (e.g., McKee and Cox 1974; Welch and Wielicki 1985; Stephens et al. 1991; Wielicki and Parker 1992). Cloud fraction is not only difficult to define because of the complex geometrical structure of clouds (Schertzer and Lovejoy 1987; Cahalan 1989; Cahalan and Joseph 1989; Coakley 1991), it also gives no information on cloud shape or internal variability. Even when shape is not an important factor, as with extensive stratocumulus decks, a minimal additional cloud parameter is some measure of the width of the probability distribution of liquid water (e.g., Lin and Rossow 1994) or of optical thickness (e.g., Pincus 1994), such as the variance of $\log(W)$, or equivalently the bounded cascade parameter f (Cahalan and Wiscombe 1993; Cahalan 1994). The present study shows that mesoscale-average albedo in ASTEX is sensitive to both A_c and f.

The current study focuses on the continuous time observations made by the National Oceanic and Atmospheric Administration (NOAA) microwave radiometer on Porto Santo Island. Porto Santo Island (33.1°N, 16.3°W) is in the Madeira Island region. This is about 900 km southeast of the Azores and 500 km north of the Canary Islands. Variations in W inferred by these observations are caused both by the advection of cloud spatial structures across the observing site and by the temporal evolution of these cloud fields. This Eulerian view is complemented by the ASTEX Lagrangian experiments that attempt to isolate the temporal evolution (see, e.g., Bretherton and Pincus 1995; Bretherton et al. 1995a), as well as by ASTEX satellite studies that clarify the synoptic situation (e.g., Bretherton et al. 1995b).

The outline of the paper is as follows. Section 2 describes the microwave radiometer data, the separation of the data into "clear" and "cloudy" segments, and the identification of an 8-day subset of mainly stratocumulus clouds. Section 3 describes the diurnal cycle in the various cloud parameters derived from the ASTEX microwave dataset and from the 8-day subset. Section 4 discusses the diurnal cycle in cloud reflectivity, in the plane-parallel albedo bias during ASTEX, and during the 8-day subset, and compares these to the same quantities found previously in FIRE. Finally, section 5 summarizes the results and discusses their implications.

2. Data

Measurements from Porto Santo were taken at 10 Hz and averaged over 30-s intervals by the NOAA upward-looking three-channel microwave radiometer during 1–28 June 1992. The microwave channels at 20.6 and 31.65 GHz are used to estimate the cloud liquid water path. The accuracy of these estimates has been discussed by Snider (1988) and Albrecht et al. (1990) in relation to measurements of primarily stratocumulus cloud during FIRE, and the instrument itself is described in Hogg et al. (1983). A precipitation flag is provided with the data to indicate occasions when the antenna reflector is wet due to rain or condensation and therefore may not be representative of nonprecipitating cloud. More than 78 000 observations were made during the 28-day period, and fewer than 700 (0.9%) were discarded due to precipitation. While the noise level for a single measurement is around 20 g m^{-2}, grouping the data for the histogram analysis discussed later reduces this uncertainty by the square root of the number of observations in each bin.

To perform an analysis of the ASTEX data, it was necessary to define a threshold level to separate the data into clear and cloudy regions. To maintain consistency with the FIRE study, the same assumption was made

to establish the cloud–clear threshold at 10 g m^{-2}; values below this level are considered "cloud free." Hourly cloud fractions for all 28 days were determined; a histogram of this result is displayed in Fig. 1a. A wide distribution of hourly cloud fractions exist, indicative of the more complex atmospheric conditions of the ASTEX region including vertically developed cumulus and cirrus cloud. The mean cloud fraction for the entire set of data is 50%. To examine the sensitivity of cloud fraction to threshold specification, the same calculations were performed with a lower threshold of 6 g m^{-2}. For this decreased threshold, mean cloud fraction for the 28 days rose to 58%. This is a substantial increase for such a small shift in threshold and is related to the existence of numerous small liquid water amounts.

To isolate those days within the 28-day ASTEX study that appeared to be similarly insensitive to the threshold, as in the FIRE cases, a criterion of "threshold insensitivity" was established to identify appropriate days. The criterion is that *the cloud fraction increases by less than 8% as the threshold is lowered from 10 to 6 g* m^{-2}. This criterion is important because it serves to eliminate from consideration those days where the exact placement of the threshold has an impact on the determination of key parameters as large as it does when all 28 days are considered. The 8 accepted days by this criterion are 1, 12, 13, 17, 18, 21, 22, and 24 June. As one might expect, these days tend to have thicker clouds and larger cloud fractions. Specifically, on the threshold-insensitive days 1) clouds are thicker, so that $\overline{\log(W)} > 1.5$, and 2) cloud fraction exceeds the mean, so that $A_c \geq 50\%$. Four other days also satisfied these two conditions but failed the threshold insensitivity criterion. Over 22 000 observations (29% of the 28 day total) are included in the 8-day subset. Using the 10 g m^{-2} threshold throughout, histograms of hourly cloud fraction for this 8-day subset are displayed in Fig. 1b and hourly cloud fractions for the 18 days of the FIRE-I campaign are shown in Fig. 1c. It is readily apparent that the 8-day subset of hourly cloud fractions more closely resembles the FIRE case than the 28-day ASTEX set, with a greater percentage of hours having the largest cloud fractions and decreased percentages of both zero and intermediate cloud fraction values.

The contrast between the three groups of data is clearly defined in Fig. 2, which displays the cumulative distribution of the duration in minutes of series of consecutive cloud-free observations. (Note that this is *not* merely a cumulative distribution of hourly clear fraction, which is computable from Fig. 1; it is a cumulative distribution of the *durations* of clear intervals.) The solid lines are from the 28-day ASTEX set, the dashed lines are from the 8-day subset, and the dotted lines are from the 18 days of FIRE. Two normalizations are shown for each line: the upper three curves are normalized by the total duration of all clear observations, so that each reaches a maximum of 100% at the largest

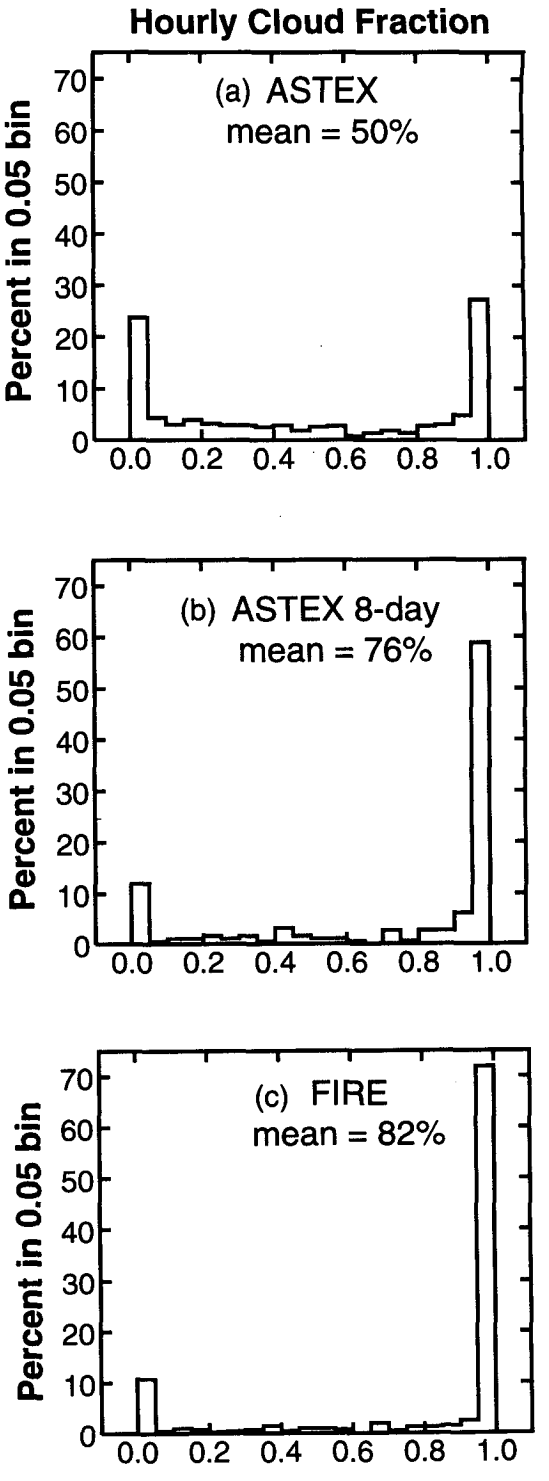

FIG. 1. Histogram of hourly cloud fractions derived from microwave radiometer measurements in (a) the June 1992 ASTEX observations on Porto Santo in the Azores; (b) the 8-day ASTEX subset defined in the text; and (c) the July 1987 FIRE observations on San Nicolas Island. In all cases, cloud fraction is defined to be the fraction of time the liquid water path exceeds 10 g m^{-2}. To facilitate comparison of the three cases, the counts in each bin have been multiplied by 100/*N*, with *N* the total number of counts, so that each bin gives the percentage of total counts.

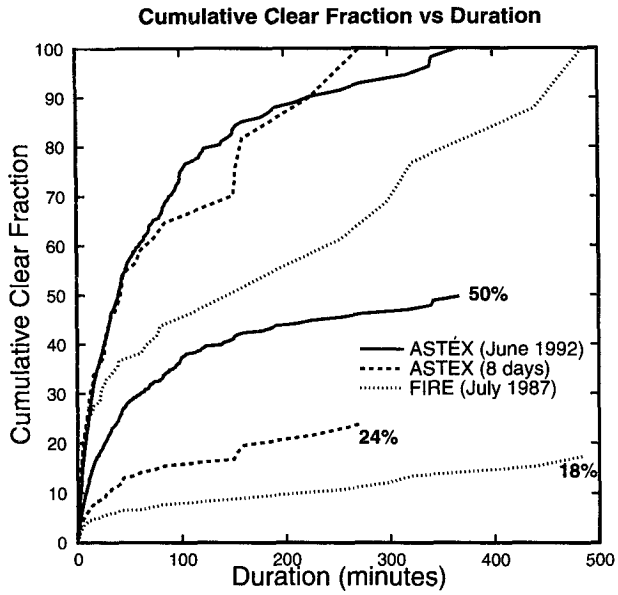

FIG. 2. Cumulative distribution of the duration in minutes of series of consecutive cloud-free observations. The same 10 g m^{-2} threshold is used as in Fig. 1. The solid lines are from the 28 days of ASTEX; the dashed lines are from the 8-day subset discussed in the text; and the dotted lines are from the 18 days of FIRE. Two normalizations are shown for each line. The upper three curves are normalized by the total duration of all clear observations, so that each reaches a maximum of 100% at the largest observed duration. The lower three curves are normalized by the total duration of all observations and thus reach a maximum equal to the overall clear fraction, which is 50% for ASTEX, 24% for the 8-day subset, and 18% for FIRE.

observed duration. The lower three curves are normalized by the total duration of all observations and thus reach a maximum equal to the overall clear fraction values of 50% for ASTEX, 24% for the 8-day subset, and 18% for FIRE. The "clear" regions over Porto Santo were generally of much shorter duration than in FIRE, with 50% lasting less than 40 min. In comparison, only 37% of the cumulative clear fraction in FIRE is of 40-min duration or less. This distinction in gap distribution may be directly related to differences in cloud type with more temporally variant vertically developed cumulus in the ASTEX region compared with the more horizontally extensive cloud cover of a coastal Californian stratocumulus regime.

3. Cloud parameters

To determine the cloud parameters needed to estimate the cloud reflectivity, we need to compute the mean and variance of the logarithm of the cloud liquid water path, as discussed in Cahalan et al. (1994a). We illustrate this first for the distribution of liquid water path from all 30-s average microwave measurements made during ASTEX, and then for the 8-day subset. Although there is cloud structure not resolved by the 30-s averaging time, studies in California stratocumulus observed in FIRE-I (e.g., Cahalan and Snider 1989) show that there is much less variability at the higher frequencies, which thus should not strongly affect cloud parameters determined from the low-order moments of the one-point distributions. However, we shall

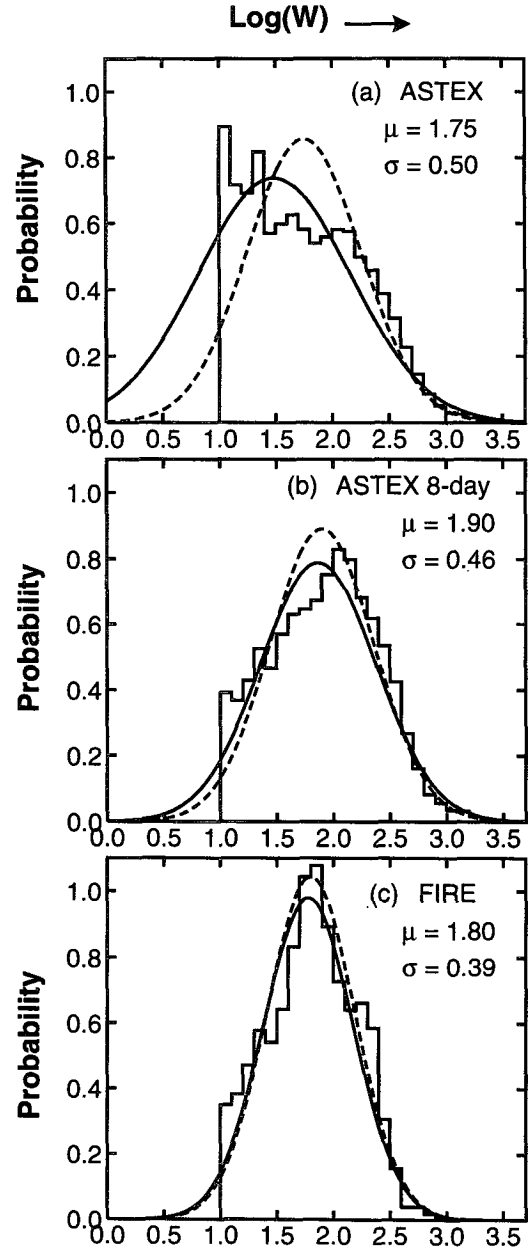

FIG. 3. Histograms of liquid water path W for (a) ASTEX, (b) the 8-day subset described in the text, and (c) FIRE. Only values exceeding 10 g m^{-2} are included. To provide a common normalization, each histogram bin was multiplied by $1/Ndx$, with N the total number of counts above the threshold, and dx the bin width, so that the result integrates to unity, like a probability density. The listed μ and σ are the mean and standard deviation of the binned values. The standard deviation σ determines the fractal parameter f. The smooth curves are lognormal, with parameters determined as discussed in the text.

see that these parameters are likely to be affected by the high frequency of thin cloudiness, observed in ASTEX down to the detectability threshold of the microwave radiometer, but not in FIRE-I.

Figure 3a shows a histogram of $\log(W)$ for all ASTEX measurements for which $W \geq 10$ g m^{-2}, the threshold value discussed in the preceeding section. These values of $\log(W)$ have a mean of $\mu = 1.75$ and a standard deviation of $\sigma = 0.5$ [which corresponds to fractal parameter $f = 0.62$, as discussed in Cahalan (1994c)]. A lognormal having the same values of μ and σ and the same fraction above threshold is shown by the dashed curve in Fig. 3a. This fits the tail of the observed distribution above 150 g m^{-2} quite well but badly misses the observed peak at the low end, resulting in a large total squared error, or χ^2, exceeding 4500 for the 28 bins.

The histogram in Fig. 3a shows a large probability near the cloud threshold, suggesting the existence of a large fraction of cloudiness below the threshold, which may greatly impact any estimates of cloud parameters. To quantify the impact of subthreshold cloudiness on cloud parameters requires that the probability distribution be extrapolated below the threshold. Since the dashed curve is sensitive only to the mean and variance, not the shape of the distribution, it is unlikely to provide a good extrapolation. The solid curve is a lognormal fit to the histogram in which μ, σ and the norm are freely varied so as to minimize χ^2, which is thus reduced to less than 2000. This fit does better than the dashed curve at the low end, although it underestimates the fraction of thicker cloud. The important point is that the estimated mean of the fit, $\mu = 1.49$, is much smaller than the mean of the data, while the estimated standard deviation of the fit, $\sigma = 0.67$ (which corresponds to $f = 0.79$), is much larger.

Despite the inaccuracy of the least squares fit, let us nevertheless imagine for a moment that the solid curve is the true distribution of $\log(W)$, in order to determine the accuracy of the estimated cloud fraction. The fraction of the curve's area above the 10 g m^{-2} threshold computed from the cumulative distribution is about 0.765, and this must correspond to the observed 50% of the data exceeding the threshold, so that the *true* cloud fraction A_c(true) must satisfy $0.765\ A_c(\text{true}) \approx 50\%$ or $A_c(\text{true}) \approx 65\%$. In other words, the portion of thin cloud below the threshold accounts for an additional 15% cloud fraction, not included in the 50% cloud fraction detectable by the radiometer. This can be roughly verified by lowering the threshold to 6 g m^{-2}. In that case, 0.85 of the curve's area and 58% of the data exceed the threshold, so that $0.85\ A_c(\text{true}) \approx 58\%$ or $A_c(\text{true}) \approx 68\%$; in other words, 10% of the cloud fraction is subthreshold. Of course, the true distribution is unknown and not likely to be a simple lognormal. However, this exercise clearly indicates the extent to which the simple threshold estimate of "cloud fraction" may underestimate the true cloud fraction when one includes the days in ASTEX having very thin cloud.

Figure 3b shows the same distribution and fits as in Fig. 3a but now restricted to the 8 "thick cloud" days, determined as discussed in the preceding section. In this case the dashed curve having the same values of $\mu = 1.9$ and $\sigma = 0.46$ as the data has $\chi^2 = 856$, while the solid curve has nearly identical values of $\mu = 1.87$ and $\sigma = 0.51$ but slightly reduced $\chi^2 = 627$. If the solid curve is the true distribution, we find $0.955\ A_c(\text{true}) \approx 76\%$, so that $A_c(\text{true}) \approx 80\%$. Thus, the threshold approach underestimates the cloud fraction by only 4%, due to the small fraction of cloud that is thinner than the threshold. The decreased threshold sensitivity indicates that the estimates of cloud parameters for the 8 thick cloud days are more trustworthy than those for the full 28 days.

The 1987 FIRE observations had a smaller fraction of thin cloud, as shown in Fig. 3c. In this case the dashed curve has mean and standard deviation $\mu = 1.8$ and $\sigma = 0.39$, as does the data, and $\chi^2 = 1045$, while the solid curve has nearly identical values of $\mu = 1.78$ and $\sigma = 0.40$, and slightly reduced $\chi^2 = 956$. If the solid curve is the true distribution, then $0.975\ A_c(\text{true}) \approx 82\%$, so that $A_c(\text{true}) \approx 84\%$, and the threshold approach underestimates the cloud fraction by only 2%. Thus, the cloud parameters estimated from 18 days in FIRE, discussed in Cahalan et al. (1994a), are less sensitive to the threshold than the ASTEX results discussed here.

Observations made during a given hour of the day may be composited over all 28 days, or over the 8-day thick cloud subset, thus producing a histogram like those in Fig. 3 for each hour of the day. This averages out interdiurnal variations such as those discussed by Gollmer et al. (1995). The histogram for each hour may be characterized by 1) the cloud fraction or fraction of values above the $W = 10$ g m^{-2} threshold, 2) the mean $\mu \equiv \overline{\log(W)}$, and 3) the variance $\sigma^2 \equiv \overline{(\log(W) - \mu)^2}$. As discussed in Cahalan et al. (1994a), σ determines the fractal parameter f for a cascade having a probability distribution that is lognormal-like near the mean but vanishes outside a finite range. The cascade also produces a power-law wavenumber spectrum, as observed in FIRE (Cahalan and Snider 1989). The parameters f and μ then determine the mean of W, which is related to the mean vertical optical thickness via $\tau_v = 0.15\ W$, assuming a uniform value of effective droplet radius given by $r_{\text{eff}} = 10\ \mu$m. [For discussion of variations in r_{eff}, see Fairall et al. (1990) and Nakajima et al. (1991). The same uniform value is assumed in Cahalan et al. (1994a) and Lin and Rossow (1994).]

The four panels in Fig. 4 show cloud parameters determined from the hourly histograms of W during ASTEX and may be compared with previous results from FIRE, given by Cahalan et al. (1994a, Figs. 8a–

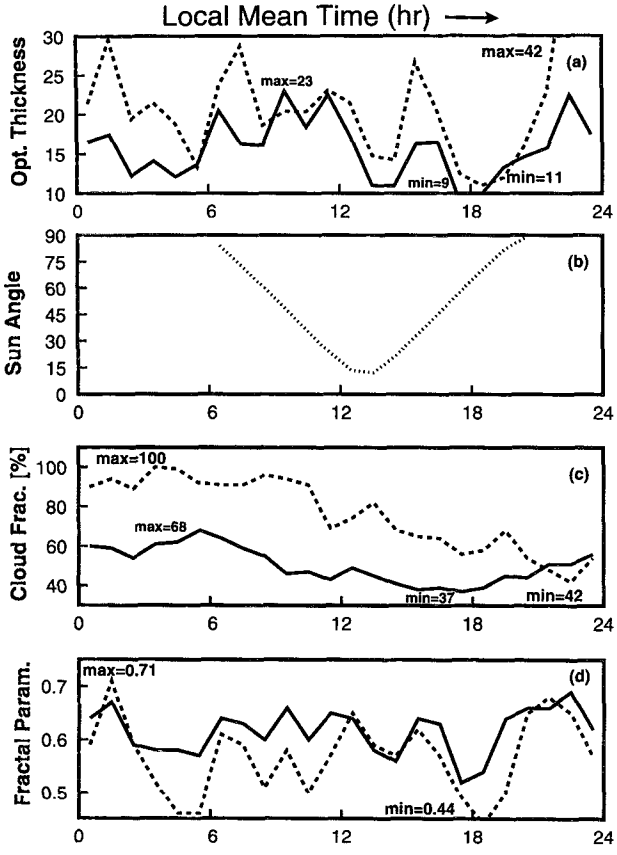

FIG. 4. Diurnal variations in (a) mean vertical cloud optical thickness (0.15 times cloud liquid water path W); (b) solar zenith angle (for Porto Santo Island in June); (c) stratocumulus cloud fraction (from fraction with $W > 10$ g m^{-2}); and (d) fractal parameter [from Stdev(log$W$)]. The solid lines in (a), (c), and (d) are determined by compositing histograms of W for each hour of the day during the 28-day period of ASTEX, while the dashed lines are from composites of the 8-day ASTEX subset described in the text. The same quantities for FIRE are given in Fig. 8 of Cahalan et al. (1994a).

d). Figure 4a shows the values of τ_v as a function of local time (LST) for both the full 28 days of ASTEX (solid line) and for the 8-day subset (dashed line). The mean thickness of the 28-day solid line decreases from 23 at 1000 LST to 9 at 1800 LST, and the diurnal mean thickness is $\tau_v = 16$. These results are similar to the previous FIRE results using the same threshold, which decreased from 24 at sunrise to 6 at 1700 LST, with a diurnal mean of $\tau_v = 14$. If the threshold is lowered to 6 g m^{-2} in ASTEX, the maximum and minimum thicknesses decrease slightly, to 20 and 8, respectively, and the diurnal mean decreases to the same as that in FIRE, $\tau_v = 14$.

The 8-day dashed line in Fig. 4a shows a dramatic rise from a minimum of 11 at 1800 LST to 42 at 2300 LST, with a diurnal mean of $\tau_v = 21$. The large 2300 LST values suggest that there may have been precipitation events that were not flagged, because the water drops did not reach the surface. Some of the rapid variations here are probably also due to the limited 8-day sample.

Figure 4b shows the diurnal variation in the solar zenith angle at the location of the microwave radiometer on Porto Santo Island. It reaches a minimum of approximately 12° just after local noon and is similar to the variation during FIRE.

Figure 4c gives the diurnal variation in cloud fraction, with the 28-day solid line decreasing from 68% near sunrise to 37% in late afternoon, with a mean of 51%. Again, we emphasize that the 28-day cloud fractions would be much larger with a lower threshold. The 8-day dashed line in Fig. 4c decreases from 100% before sunrise to 42% at 2300 LST, and has a mean of 76%. By contrast, in FIRE, cloud fractions remained near 100% until 1100 LST, then fell to a minimum of 57% at 1600 LST, rose again in the evening, and averaged 82%. The fact that cloud fractions at sunrise and sunset are smaller in ASTEX than in FIRE has a significant impact on the albedo bias, as seen in the next section.

Finally, Fig. 4d shows the fractal parameter, which generally fluctuates in phase with the mean thickness and has a diurnal mean value of $f = 0.62$ for the 28 days, corresponding to $\sigma = 0.5$. The 8-day subset has a wider range, $f = 0.44$ to 0.71, but a similar diurnal mean, $f = 0.57$, corresponding to $\sigma = 0.45$. The largest fractal parameter observed in FIRE was about equal to the daily mean in ASTEX, $f \approx 0.6$, but in FIRE this was reached only at about 0600 LST. A positive correlation between τ_v and f was observed earlier in FIRE, though no simple proportionality appears to hold.

4. Plane-parallel albedo bias

The cloud albedo as a function of local time may be estimated from the cloud parameters given in Figs. 4a–d, using the independent pixel approximation (Cahalan et al. 1994a). This simply involves integrating over a distribution of cloud optical depths and assumes that net horizontal photon transport may be neglected when computing average flux over the mesoscale, which has been verified for bounded cascades (Cahalan et al. 1994b). The resulting cloud albedos for ASTEX, the 8-day subset, and FIRE are shown in Fig. 5a. Multiplying the cloud albedo by the cosine of the solar zenith angle gives the cloud reflected flux in units of the solar beam intensity (Fig. 5b). The average cloud albedos are uniformly larger by 0.05 or more for the 8-day subset than for the full 28 days. This albedo difference is largest at 0800 and 1600 LST when the thickness difference in Fig. 4a is largest. Cloud thickness during FIRE has about the same mean as the 28 days of ASTEX and thus nearly the same cloud albedo, though the greater cloud fraction in FIRE implies larger mesoscale average albedo when clear sky is included in the average.

While the cloud albedo itself (Fig. 5a) depends mainly on the values of mean cloud optical thickness

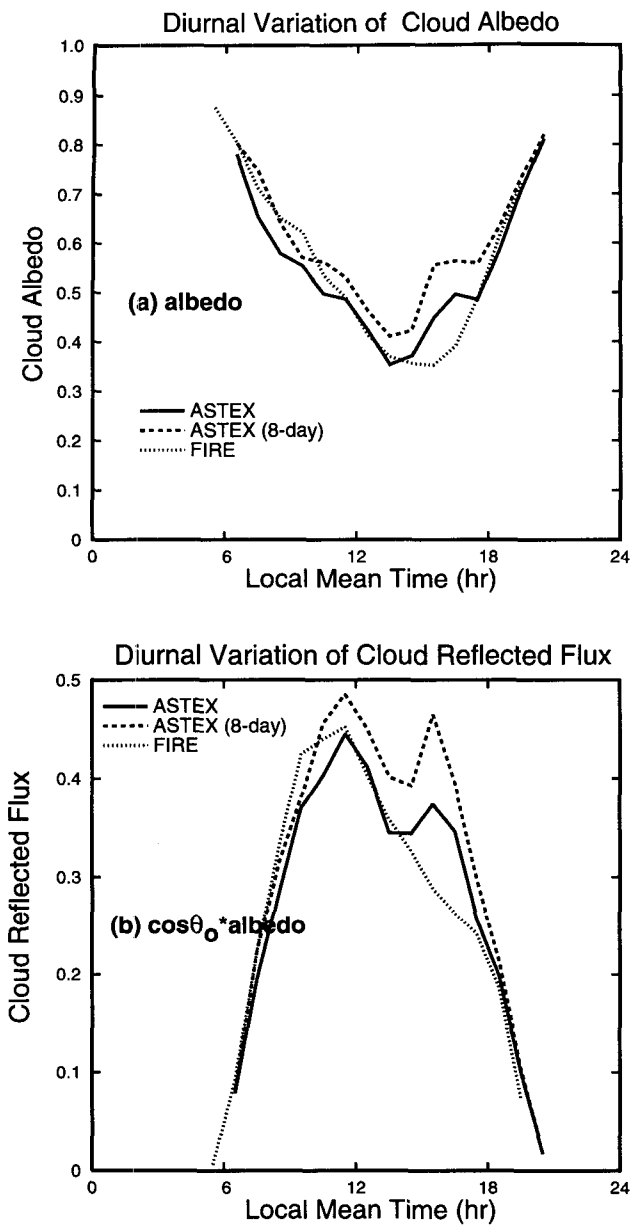

FIG. 5. (a) Diurnal cycle of cloud albedo computed by the independent pixel approximation for ASTEX and the 8-day ASTEX subset discussed in the text, with the parameters from Fig. 4, and also for FIRE, with the parameters given in Fig. 8 of Cahalan et al. (1994a). (b) The diurnal cycle of the reflected flux in units of the solar beam intensity, or equivalently cosine of the solar zenith angle times the cloud albedo, computed as in (a) for ASTEX, the 8-day ASTEX subset, and FIRE.

and solar zenith angle given in Figs. 4a,b, corrections to the albedo associated with inhomogeneity, the albedo biases, depend primarily on the cloud fraction and fractal parameter given in Figs. 4c,d. The total albedo bias is defined as follows: the albedo of the average optical thickness, the average being taken over both clear and cloudy regions, minus the average of the albedos, including both the clear-sky albedo and the probability distribution of cloud albedo.

Current practice is to approximate the average of the albedos by the sum of a single cloud albedo times the cloud fraction plus a clear albedo times the clear fraction. With this approximation, the total albedo bias reduces to a contribution depending only on cloud fraction. It may be written in terms of the reflectance R as a function of mean vertical cloud optical thickness τ_v, as follows:

$$B(A_c) \equiv R(A_c\tau_v) - [A_cR(\tau_v) + (1 - A_c)R(0)], \tag{4.1}$$

where A_c is the cloud fraction, $R(0)$ is the clear-sky reflectance, and the dependence of R on solar zenith angle and microphysical parameters has been suppressed. Note that the cloud is assumed to be thinner by a factor A_c in the first term. This is so that the mean thickness for the uniform cloud is identical to the mean over *both* clear and cloudy regions of the fractional cloud case. This also implies identical total cloud liquid water. The term $B(A_c)$ will be referred to as the "cloud fraction bias." Although each of the two terms in Eq. (4.1) depend upon τ_v, the difference has only a weak dependence, which has thus been suppressed. [The insensitivity of the bias to τ_v occurs because the curvature of $R(\log(\tau))$ is small, as shown in Cahalan et al. (1994a).]

Real clouds, however, do not have a uniform cloud albedo, and thus, there is an additional contribution to the total albedo bias, which may be written as follows:

$$B(f) \equiv A_c\left[R(\tau_v) - \int_0^\infty R(\tau)p(\tau)d\tau\right], \tag{4.2}$$

where $p(\tau)$ is the full probability distribution of cloud optical thickness τ normalized to integrate to unity. Note that the distribution of optical thickness in the clear sky is not included in $p(\tau)$. Here $p(\tau)$ will be approximated by the histograms of W shown in Figs. 3a–c, assuming $\tau = 0.15W$. The term $B(f)$ will be referred to as the "fractal structure bias," and again its weak dependence on τ_v is suppressed.

The total albedo bias is the sum of $B(A_c)$ and $B(f)$. Note that both contributions represent biases in the *area-averaged* albedo, not only the cloud albedo. In particular, $B(f)$ here is averaged over the full area and is thus weighted by the cloud fraction. Nevertheless, it makes a significant contribution to the total, as will be seen below. There may also be an additional contribution from 3D radiative effects, which has been termed the "independent pixel bias." However, this tends to be small for area-average fluxes over stratocumulus clouds (Cahalan et al. 1994b).

The clear-sky albedo will be neglected in the following so that

$$R(0) = 0. \tag{4.3}$$

This is a reasonable approximation over dark ocean surfaces, as long as the solar zenith angle is not too large. However, when the sun approaches the horizon, the clear-sky albedo can become quite large, due not only to surface reflection but also to haze and clouds that are too small and/or too thin to be observed. As a result, satellite threshold estimates of cloud fraction more often misclassify clear pixels as cloudy near the limb than near the zenith. Such methods estimate an "effective cloud fraction" that differs from the actual fraction by a "limb bias" having a zenith angle dependence resulting from the distribution of subresolution clouds and haze, etc. In contrast, here the cloud fraction is known from the cloud liquid water distribution, but the estimated albedo has a limb bias due to inaccuracies in the assumed clear-sky albedo at large angles. This can make a large contribution to the total albedo bias if there is significant clear sky at sunrise and sunset. However, since the incident solar flux is approaching zero at sunrise and sunset, as seen in Fig. 5b, the large limb bias in albedo will be found to have little impact on the bias in reflected flux.

The diurnal cycle of albedo bias for the 28 days of ASTEX is shown in Fig. 6a, a plot of the total bias (solid line), as well as the contributions from $B(A_c)$ (dotted) and $B(f)$ (dashed), versus local mean time in hours. These may be compared with previous results from FIRE, given by Cahalan et al. (1994a, Fig. 9). A large limb bias is found at both sunrise and sunset, when the total exceeds 0.3. This effect was seen only at sunset in FIRE, since very little clear sky occurs in FIRE until after 1000 LST. The total albedo bias for ASTEX also has a 1000 LST maximum of about 0.3, due mostly to a cloud fraction contribution of 0.2, also absent in FIRE because of the large cloud fraction at 1000 LST. The total albedo bias for ASTEX has a second maximum of about 0.2 at local noon, again mainly from the cloud fraction contribution. The total then drops to a minimum of about 0.1 at 1400 LST, when cloud fraction and fractal structure contribute about equally. Finally, a third maximum due to cloud fraction occurs at 1600 LST. The fractal structure contribution is slightly smaller in ASTEX than in FIRE, because the lower values of A_c more than offset the larger values of f. Although still not negligible, the importance of the within-cloud fractal structure is secondary to that of the cloud fraction, when all 28 days of ASTEX are considered.

The total albedo bias in the 8-day subset is shown in Fig. 6b and behaves quite differently than the 28-day bias. The cloud fraction for the 8 days remains above 90% until after 1000 LST, as seen earlier in Fig. 4c, and as a result, the bias at 1000 LST becomes dominated by the fractal structure, as in FIRE. There remains a noon maximum in the cloud fraction contribution, but this now receives a roughly equal contribution from the fractal structure. The 1400 LST minimum bias is mainly due to fractal structure. Finally, the 1600 LST

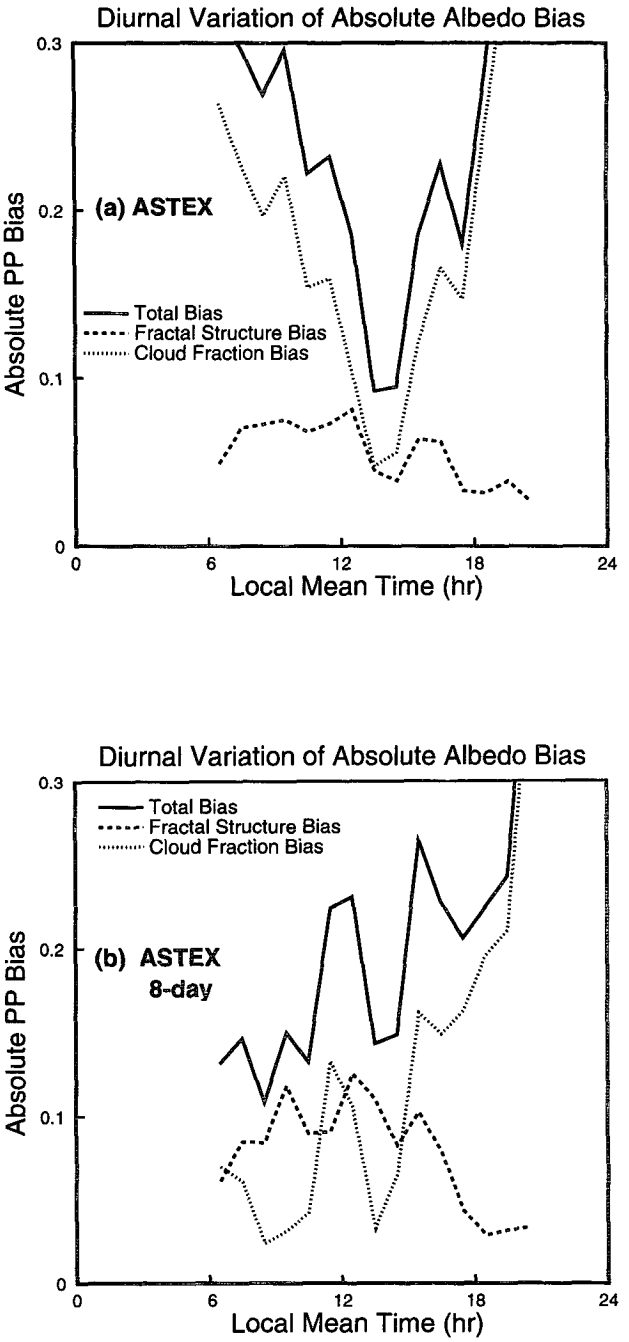

FIG. 6. (a) Diurnal cycle of absolute plane-parallel bias in area-averaged albedo for ASTEX. (b) The 8-day ASTEX subset discussed in the text, computed from the respective cloud parameters shown in Fig. 4. The dotted curve is the contribution due to the cloud fraction, using only plane-parallel computations, computed as in Eq. (4.1). The dashed curve is the additional bias associated with the within-cloud fractal structure, computed using the histograms in Fig. 3, as in Eq. (4.2). The sum of the dotted and dashed curves equals the total plane-parallel albedo bias given by the solid curve. The same quantities for FIRE are given in Fig. 9 of Cahalan et al. (1994a). Subtracting the total albedo bias, as shown by the solid curves in (a) and (b), from the plane-parallel albedo gives the area-averaged albedo, equal to the cloud fraction times the cloud albedo shown in Fig. 5a (the solid and dashed curves, respectively).

maximum and the evening limb bias are mainly from the cloud fraction, similar to those of the full 28-day set. These contrasting results from ASTEX, the 8-day subset, and FIRE show that cloud fractal and radiative properties can vary considerably from one site and time to another, and even within the same site, as meteorological conditions vary.

Multiplying the albedo bias in Figs. 6a,b by the cosine of the solar zenith angle gives the bias in the area-averaged reflected flux. The resulting diurnal cycle in the reflected flux bias for the full 28 days of ASTEX is shown in Fig. 7a, and that for the 8-day subset is shown in Fig. 7b. The limb bias in the albedo is now suppressed, since there is little incident solar flux at sunrise and sunset. The peaks that occur at 1000 LST, noon, and 1600 LST in the albedo bias in Fig. 6a are also the dominant features of the reflected flux bias in Fig. 7a, and similarly the noon and 1600 LST peaks in Fig. 6b dominate the total reflected flux bias in Fig. 7b. Just as in Fig. 6a, the main contribution in Fig. 7a comes from the cloud fraction, although the fractal structure contribution is not negligible. Just as in Fig. 6b, the two contributions to the flux bias in Fig. 7b are comparable in the noon and 1600 LST peaks, while the fractal structure dominates in the morning and at the 1400 LST minimum, and the cloud fraction dominates in the evening.

5. Results and discussion

The main results of this study are summarized as follows.

1) When cloud fraction is defined by a threshold of $W = 10$ g m^{-2}, identical to that used in a previous study of FIRE data, the diurnal mean cloud fraction during ASTEX equals 50%, while that of a selected 8-day subset is 76%, compared to 82% during FIRE. Cloud fraction is sensitive to the threshold for the 28 days but not for the 8 days or for FIRE.

2) "Clear" regions over Porto Santo were generally of much shorter duration than in FIRE, with 50% lasting less than 40 min, with roughly the same distribution seen during the 8-day subset, while 50% lasted longer than 140 min in FIRE.

3) The diurnal mean W in ASTEX slightly exceeds that observed in FIRE, 107 g m^{-2} compared to 92 g m^{-2}, but there is a larger percentage of both larger and smaller values, resulting in a larger variance of $\log(W)$, 0.50 compared to 0.39, but a smaller mean of $\log(W)$, 1.75 compared to 1.80. The 8-day subset has the same fraction of large values as the full 28 days, but the fraction of small values is reduced to roughly the same as in FIRE, resulting in a larger mean W, 140 g m^{-2}, and a larger mean and variance of $\log(W)$, 1.9 and 0.46, than in FIRE.

4) The diurnal cycle in cloud fraction in ASTEX has a morning peak of approximately 70% and falls to less than 40% in late afternoon. The morning peak in the 8-day subset is close to 100%, as in FIRE, but unlike FIRE there is a local minimum of about 50% at local

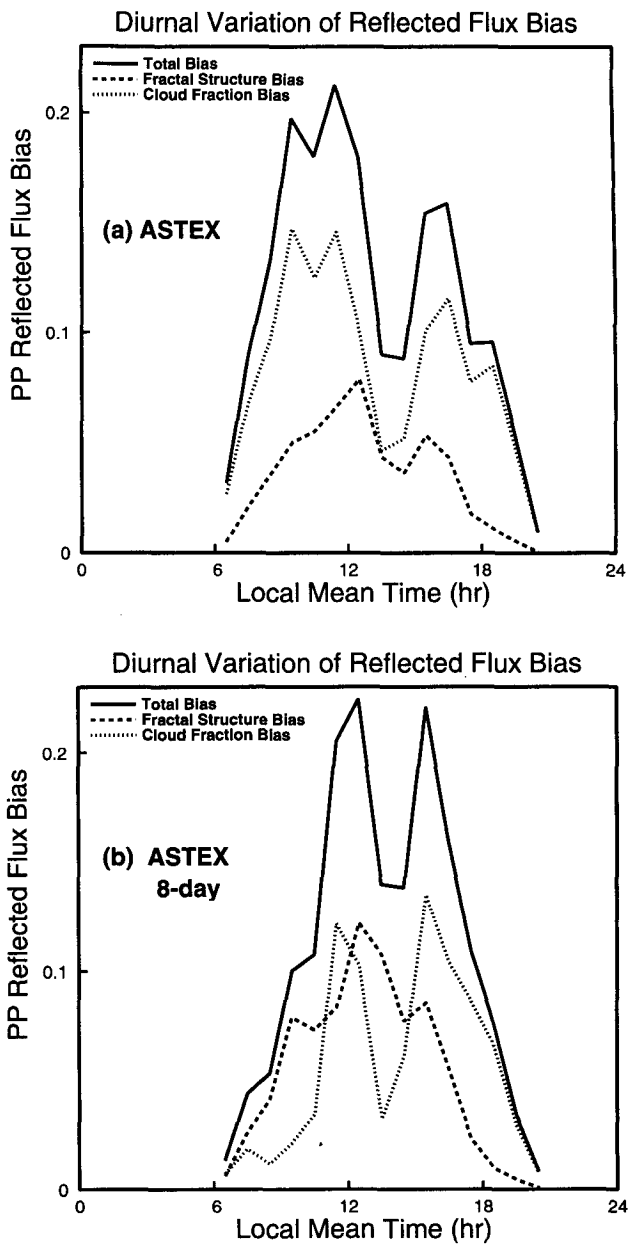

FIG. 7. (a) Diurnal cycle of absolute plane-parallel bias in area-averaged reflected flux for ASTEX. (b) The 8-day ASTEX subset discussed in the text, computed by multiplying the zenith angle shown in Fig. 4b by the respective albedo biases shown in Figs. 6a,b. As in Fig. 6, the dotted curve is the contribution due to the cloud fraction, while the dashed curve is the additional bias associated with the within-cloud fractal structure, and the sum of the dotted and dashed curves equals the total flux bias given by the solid curve. Subtracting the total flux bias shown in (a) and (b) from the plane-parallel flux gives the area-averaged reflected flux, equal to the cloud fraction times the cloud reflected flux shown in Fig. 5b (the solid and dashed curves, respectively).

noon and an absolute minimum of 42% at 2300 LST, much lower and later than the 57% minimum seen at 1600 LST in FIRE.

5) The diurnal cycle in the plane-parallel albedo bias during ASTEX is more sensitive to the cloud fraction than it is to the within-cloud fractal structure and is dominated by the limb bias associated with the treatment of the clear-sky albedo as the sun approaches the horizon at sunrise and sunset. However, the flux bias is quite small then, since there's not much solar flux to reflect at that time. Thus, the largest reflected flux bias occurs in midday and has maxima at maxima of the albedo bias. The diurnal cycle in the bias for the 8-day subset is similar to that of FIRE except it has an additional noon peak in the cloud fraction contribution, which raises the bias to 0.2, roughly twice the midday peak observed during FIRE.

The ASTEX observations on which these estimates are based were affected by the relatively high percentage of very thin cloud. Extrapolation of the LWP histogram using a lognormal fit suggests that 15% additional cloud fraction is below the threshold of detectability of the microwave radiometer. Sensitivity of cloud fraction to threshold is a common problem that often arises due to the ubiquity of thin clouds and of cloud structure not resolved by the observing instrument. Here we have focused on the estimation of cloud albedo, and find that the results for the full 28 days of ASTEX, shown in Fig. 5a, are sensitive to cloud fraction, especially as the sun approaches the horizon. Removal of this limb bias will require careful treatment of the so-called clear sky to include effects of haze and thin cloud, as well as subresolution cumulus.

The threshold problem is less severe for the 8-day subset and FIRE, which have relatively well-defined cloud fractions. In the morning, when cloud fractions approach 100%, the cloud albedo (Fig. 5b) and the albedo bias (Fig. 6b) are nearly equal in the two cases. However, the local minimum in cloud fraction that occurs at noon in ASTEX, and is most noticable for the 8-day subset, as seen in Fig. 4c, contributes a noontime maximum to the albedo bias equal to the fractal structure contribution, as we have seen in Fig. 6b. Recall, however, that these bias estimates are based on the independent pixel approximation, which neglects net horizontal photon transport (Cahalan et al. 1994b). That approach is most trustworthy when the cloud fluctuations are separated by more than a photon mean free path. This was justified in FIRE because of the steep falloff of the power spectrum of cloud liquid water. The shorter duration of the clear fractions in ASTEX suggests that 3D radiative effects may be more important here.

The sensitivity of the mesoscale albedo to the variance of $\log(W)$ shows that this quantity is as important as cloud fraction in modeling the current climate and can be more important in some situations. The fact that it exhibits significant diurnal variations in both FIRE and ASTEX suggests that it may also play an important role in climate change. Efforts are under way to allow climate models to predict cloud liquid water in each grid box (e.g., Sundqvist et al. 1989). Fractal models have suggested parameterizations of both the variance and resolution dependence of subgrid-scale liquid water in marine stratocumulus, as determined by the parameters f and c in the bounded cascade model (e.g., Cahalan 1994c). These boundary layer clouds cover as much as 25% of the earth's surface (Hartmann et al. 1992) and are major contributors to cloud radiative forcing (Ramanathan et al. 1989; Harrison et al. 1990). More research is needed on the structure and variability of clouds having significant vertical development (see, e.g., Chertock and Fairall 1993). These are present on many days of the ASTEX study. Compilation of a complete climatology of cloud structure parameters, detailing their diurnal, seasonal, and geographic dependence, is an important task for the future (see, e.g., Lin and Rossow 1994).

Acknowledgments. Support from NASA Contracts NAS5-30430 and NAS5-30440 and DOE ARM Grant DE-A105-90ER61069 is gratefully acknowledged. The authors thank A. J. Francavilla and D. A. Hazen of the NOAA Environmental Technical Laboratory for their assistance in performing the radiometric observations at Porto Santo Island.

REFERENCES

Albrecht, B. A., C. W. Fairall, D. W. Thomson, A. B. White, J. B. Snider, and W. H. Schubert, 1990: Surface-based remote sensing of the observed and the adiabatic liquid water content of stratocumulus clouds. *Geophys. Res. Lett.*, **17,** 89–92.

Bretherton, C. S., and R. Pincus, 1995: Cloudiness and marine boundary layer dynamics in the ASTEX Lagrangian experiments. Part I: Synoptic setting and vertical structure. *J. Atmos. Sci.*, **52,** 2707–2723.

——, P. A. Austin, and S. T. Siems, 1995a: Cloudiness and marine boundary layer dynamics in the ASTEX Lagrangian experiments. Part II: Cloudiness, drizzle, surface fluxes and entrainment. *J. Atmos. Sci.*, **52,** 2724–2735.

——, E. Klinker, A. K. Betts, and J. A. Coakley Jr., 1995b: Comparison of ceilometer, satellite and synoptic measurements of boundary layer cloudiness and the ECMWF diagnostic cloud parameterization scheme during ASTEX. *J. Atmos. Sci.*, **52,** 2736–2751.

Cahalan, R. F., 1989: Overview of fractal clouds. *Advances in Remote Sensing Retrieval Methods,* A. Deepak, H. Fleming, and J. Theon, Eds., A. Deepak, 371–388.

——, 1994: Bounded cascade clouds: albedo and effective thickness. *Nonlinear Proc. Geophys.*, **1,** 156–167.

——, and J. H. Joseph, 1989: Fractal statistics of cloud fields. *Mon. Wea. Rev.*, **117,** 261–272.

——, and J. B. Snider, 1989: Marine stratocumulus structure. *Remote Sens. Environ.*, **28,** 95–107.

——, and W. J. Wiscombe, 1993: Impact of cloud structure on climate. *Current Problems in Atmospheric Radiation,* S. Keevallik and O. Karner, Eds., A. Deepak, 120–123.

——, W. Ridgway, W. J. Wiscombe, T. L. Bell, and J. B. Snider, 1994a: The albedo of fractal stratocumulus clouds. *J. Atmos. Sci.*, **51,** 2434–2455.

——, ——, ——, S. Gollmer, and Harshvardhan, 1994b: Independent pixel and Monte Carlo estimates of stratocumulus albedo. *J. Atmos. Sci.*, **51,** 3776–3790.

Chertock, B., C. W. Fairall, and A. B. White, 1993: Surface-based measurements and satellite retrievals of broken cloud properties in the equatorial Pacific. *J. Geophys. Res.*, **98,** 18 489–18 500.

Coakley, J., 1991: Reflectivities of uniform and broken layered clouds. *Tellus,* **43B,** 420–433.

Fairall, C. W., J. E. Hare, and J. B. Snider, 1990: An eight-month sample of marine stratocumulus cloud fraction, albedo and integrated liquid water. *J. Climate,* **3,** 847–864.

Gollmer, S., Harshvardhan, R. F. Cahalan, and J. B. Snider, 1995: Windowed and wavelet analysis of marine stratocumulus cloud inhomogeneity. *J. Atmos. Sci.,* **52,** 3013–3030.

Harrison, E. F., P. Minnis, B. R. Barkstrom, V. Ramanathan, R. D. Cess, and G. G. Gibson, 1990: Seasonal variation of cloud radiative forcing derived from the Earth Radiation Budget Experiment. *J. Geophys. Res.,* **95,** 18 687–18 703.

Hartmann, D. L., M. E. Ockert-Bell, and M. L. Michelsen, 1992: The effect of cloud type on Earth's energy balance: Global analysis. *J. Climate,* **5,** 1281–1304.

Hogg, D. C., F. O. Guiraud, J. B. Snider, M. T. Decker, and E. R. Westwater, 1983: A steerable dual-channel microwave radiometer for measurement of water vapor and liquid in the troposphere. *J. Climate Appl. Meteor.,* **22,** 789–806.

Lin, B., and W. Rossow, 1994: Observations of cloud liquid water path over oceans: Optical and microwave remote sensing methods. *J. Geophys. Res.,* **99,** 20 907–20 927.

Marshak, A., A. Davis, R. F. Cahalan, and W. J. Wiscombe, 1994: Bounded cascade models as non-stationary multifractals. *Phys. Rev.,* **E49,** 55–79.

McKee, T. B., and S. K. Cox, 1974: Scattering of visible radiation by finite clouds. *J. Atmos. Sci.,* **31,** 1885–1892.

Nakajima, T., M. D. King, J. D. Spinhirne, and L. F. Radke, 1991: Determination of the optical thickness and effective particle radius of clouds from reflected solar radiation measurements. Part II: Marine stratocumulus observations. *J. Atmos. Sci.,* **48,** 728–750.

Pincus, R., 1994: Uncertainty in cloud optical depth measurements made from satellite radiance measurements. *J. Climate,* **8,** 1453–1462.

Ramanathan, V., R. D. Cess, E. F. Harrison, P. Minnis, B. R. Barkstrom, E. Ahmad, and D. Hartmann, 1989: Cloud-radiative forcing and climate: results from the Earth Radiation Budget Experiment. *Science,* **243,** 57–63.

Schertzer, D., and S. Lovejoy, 1987: Physically-based rain and cloud modeling by anisotropic, multiplicative turbulent cascades. *J. Geophys. Res.,* **92,** 9693–9714.

Snider, J. B., 1988: Estimated accuracy of ground-based liquid water measurements during FIRE. *Proc. of FIRE Science Results 1988,* Vail, CO, NASA, 289–292.

Stephens, G. L., P. M. Gabriel, and S.-C. Tsay, 1991: Statistical radiative transport in one-dimensional media and its application to the terrestrial atmosphere. *Trans. Theory Stat. Phys.,* **20,** 139–175.

Sundqvist, H., E. Berge, and J. E. Kristjansson, 1989: Condensation and cloud parameterization studies with a mesoscale numerical weather prediction model. *Mon. Wea. Rev.,* **117,** 1641–1657.

Welch, R., and B. A. Wielicki, 1985: A radiative parameterization of stratocumulus cloud fields. *J. Atmos. Sci.,* **42,** 2888–2897.

Wielicki, B. A., and L. Parker, 1992: The determination of cloud cover from satellite sensors: The effect of sensor spatial resolution. *J. Geophys. Res.,* **97,** 12 799–12 823.